Based 3D Finite Element Analysis of a Synchronous Reluctance Motor with Sinusoidal Rotor Shape

Mbika Muteba , *Member IEEE*, Bekhi Twala, *Member IEEE* and Dan Valentin Nicolea, *Member IEEE*
School of Electrical and Electronic Engineering
University of Johannesburg, Johannesburg, South Africa

Abstract—**This paper deals with the numerical analysis of the Synchronous Reluctance Motor (SynRM) with sinusoidal rotor shape in the axial direction using the 3D Finite Element Method (FEM), and presents the airgap magnetic flux governing equation derived from Kelvin-Stoke's theorem. In the Finite Element Analysis (FEA) the airgap flux density, machines performance indexes, the torque and its ripple contents are presented. In this paper three motors having different rotor anisotropies are modelled and analyzed. The SynRM with sinusoidal rotor shape (SynRM3) FEA results are compared with the conventional SynRM without cut-off (SynRM1) and SynRM with cut-off (SynRM2) on the *q*-axis. The stator geometry of a 5.5 kW, 4-pole, 50-Hz, 8 A, conventional three-phase squirrel cage induction motor, with distributed double layer winding chorded by a single slot is used to model all three SynRMs.**

Keywords—Performance indexes, Sinusoidal rotor shape, Synchronous reluctance machine, Torque ripple, 3D Finite Element Analysis

I. INTRODUCTION

Due to their compact design and high power density, Synchronous Reluctance Motors (SynRMs) have become an interesting choice, being used as small power motors in various applications [1]. One of these applications is a small electric scooter, commonly used by people with physical disabilities. In [2] the in-wheel switched reluctance motor driving system for future electric vehicles (EVs) has been reported. A mechanical robust rotor with transverse-laminations for a synchronous reluctance machine for electric traction application is discussed in more detail in [3]. The novel lamination concept for transverse flux machines suitable for direct drive application to EVs is presented in [4]. The design optimization of SynRM drives for Hybrid Electric Vehicles (HEVs) power train application is analyzed in [5].

However, the interaction between spatial harmonics of the electrical loading and the rotor anisotropy of SynRMs causes a high torque ripple that is intolerable in most applications [6, 7]. A good number of previous work intended to reduce the torque ripple contents in SynRMs, directing their focus mostly to a suitable choice of number of flux-barriers in respect to the number of stator slots per pole per phase [8, 9], the optimization and asymmetry of the flux-barriers geometry, etc., [7, 10, 11, 12, 13]. Lately, a novel SynRM with sinusoidal rotor shape in the axial direction, without changing the flux barrier geometry, was proposed [14]. The proposed motor was shown to produce desirable results as far as torque ripple reduction is concerned. The idea in [14] was inspired and conceptualized from the work by Thomas Lipo and peers, on the material-efficient permanent magnet synchronous motor with sinusoidal magnet shape [18]. The magnet shape provides a sinusoidal magnetic flux in order to obtain better sinusoidal electromotive force, less cogging torque and smooth electromagnetic torque.

Due to the asymmetric nature of the axial geometry design of the sinusoidal lamination shape for the proposed model in [14], a comprehensive 3-D Finite Element Analysis (FEA) is needed. This is because with most electric machines with plane symmetry, the magnetic fluxes are calculated for unit depth and multiply by the stack length to find the actual magnetic flux in the machine [15, 16, 17]. It is also necessary to calculate separately the coils end-connection inductances by analytically or equivalent 2D FEM [15]. The axial variation of magnetic field is neglected and so is the effect of the various frame parts [15, 16]. For the SynRM with sinusoidal rotor shape, the *q*-axis varies along the stack length [14], which makes the field computation particularly very difficult.

This paper deals with the numerical analysis of the proposed SynRM with sinusoidal rotor shape using 3D FEM, and presents the airgap magnetic flux governing equation derived from Kelvin-Stoke's theorem. In the FEA the airgap flux density, machines performance indexes, the torque and its ripple contents are presented.

II. MOTORS SPECIFICATIONS AND DESIGN VARIABLES

It is widely known that in SynRMs the increase of the reluctance on the *q*-axis reduces the magnetizing inductance L_{mq} and further increases the saliency ratio and the inductances difference. The air to iron ratio on the *q*-axis should be taken into consideration for SynRM optimal performance. In this paper, all three rotor topologies have two flux barriers and three iron segments per pole. The main design specifications and the rotor design variables are given in Tables I and II respectively. The air to iron ratio γ_w for SynRM1 (Model without cut-off) and γ_{wc} for SynRM2 (Model with cut-off) are

$$\gamma_w = \frac{2h_b}{2h_i + h_{io}} = 0.979 \quad (1)$$

$$\gamma_{wc} = \frac{2h_b + h_c}{3h_i} = 1.487 \quad (2)$$

TABLE I: DESIGN SPECIFICATIONS

Description	Values
Stator slot Pitch ε_p	$10^o mech$
Airgap length l_g	0.88 *mm*
Stack length	160.00 *mm*
Number of barriers per pole	2
Number of pole pairs	2
Number of stator slots	36
Rotor radius R_r	48.80 *mm*
Stator radius R_s	31.62 *mm*
Shaft radius R_{sh}	24.00 *mm*
Yoke height y_h	12.87 *mm*

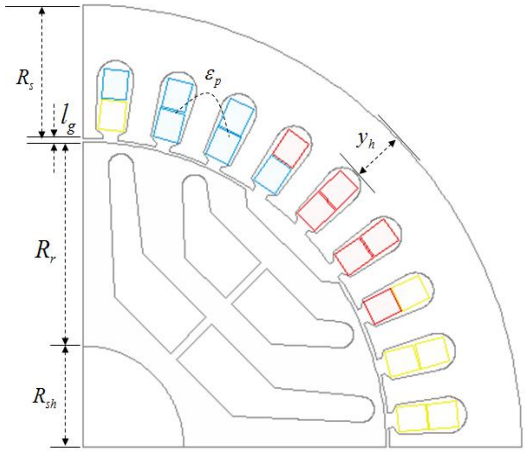

Fig.1. Cross section of the basic SynRM with cut-off on the *q*-axis

It should be noted that saturation and stator slotting are not disregarded in the FEA results, but neglected in the derivation of airgap governing expressions for the 3D Finite Element Model. The pole pitch to airgap length ratio is 188; such a ratio is acceptable. The airgap length should be kept as lower as possible, in order to increase the torque because a greater ratio provides greater saliency [19].

TABLE II: ROTOR DESIGN VARIABLES

Description	Values
Barrier height h_b	12 *mm*
Barrier width w_b	6 *mm*
Barrier pitch β_p	15° *mech*
Cut-off angle α_c	25° *mech*
Cut-off pitch τ_c	48° *mech*
Cut-off height h_c	5 *mm*
Iron width h_i	6.5 *mm*
Barrier end radius b_{er}	2.5 *mm*
Radial bridge width l_{rr}	2 *mm*
Tangential bridge width l_{tr}	2 *mm*

The rotor segments are interconnected to each other using radial bridges in the *q*-axis and tangential bridges near the airgap as shown in Fig.2. The tangential bridges hold the whole structure of the lamination together, while the radial bridges support the structure of the rotor and they are much needed especially when the SynRM is used for high speed applications. These magnetic bridges are the weakest parts in a SynRM rotor structure, since centrifugal forces are concentrated locally in the bridges. In addition, to be vulnerable to mechanical forces, the bridges will be saturated by the *q*-axis MMF during normal operation, and directly causes a torque reduction [20]. The radial bridge width l_{rr} is dependent on the mechanical limit, and the effect of radial bridges width on the saliency and inductances difference of basic SynRMs are well presented [21]. The magnetic bridges that are chosen should be thick enough to withstand the mechanical stress caused by centrifugal forces and torque. On the other hand, thinner tangential and radial bridges will result in a better electromagnetic performance. A thinner tangential bridge decreases the leakage flux as well as increases the airgap flux density due to an increase in saturation of the thinner bridges. Fig.3. (b) illustrates in 3-D view, the rotor core for the SynRM with sinusoidal rotor shape (SynRM3).

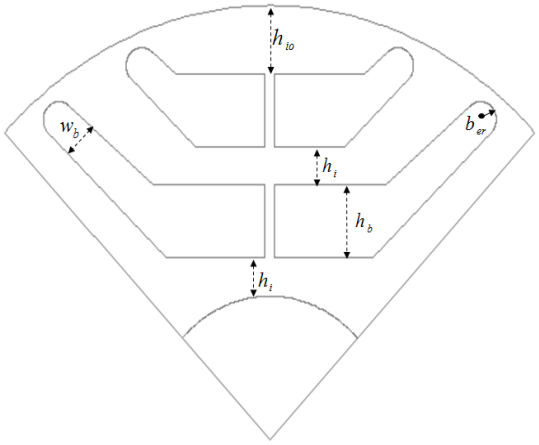

(a)

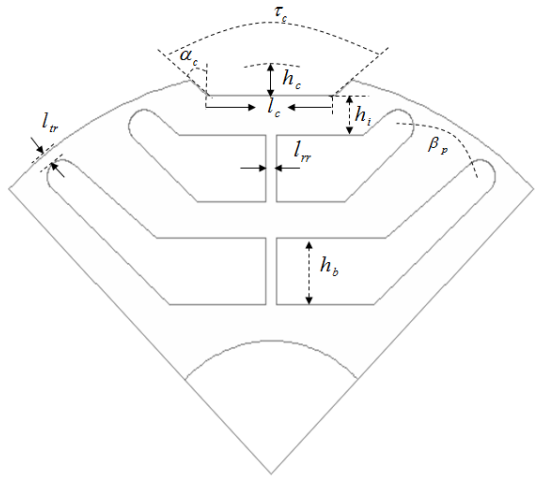

(b)

Fig.2. Basic Rotor topologies, (a) without cut-off on the *q*-axis, (b) with cut-off on *q*-axis

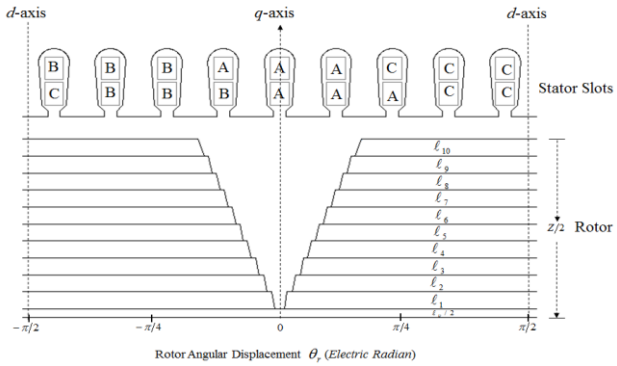

(a)

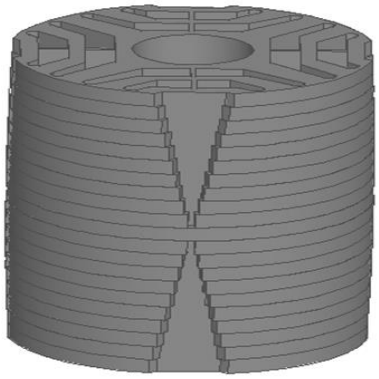

(b)

Fig.3. SynRM3 (a) cross-section of axially sinusoidal lamination rotor shape, (b) 3D view of the rotor core.

III. 3D FINITE ELEMENT MODEL

A. *Airgap magnetic flux governing expression a Template*

The rotor inner edge line in the (*x*, *y*,) plane shown in Fig. 4 (a) for a stack lamination with cut-off on the *q*-axis is a Piecewise five degree polynomial curve function $f(x) = y_{in}$. Neglecting the stator slot openings, the inner stator line is an arc curve function $f(x) = y_{ex}$. The airgap area Δg is expressed as

$$\Delta g = \int_0^{x_6} f(x, y_{ex})\,dx - \int_0^{x_5} f(x, y_{in})\,dx = \int_{C_o} f(x, y_{ex})\,ds - \int_{C_{in}} f(x, y_{in})\,dS \quad (1)$$

The line integral in (1) that determines the airgap area of a stack rotor lamination with cut-off on the *q*-axis can be converted to a simpler form by using the Green's theorem. From Fig. 4 (a), C_o is the outer arc curve and C_{in} is a summation of two arc functions and three straight line functions. The curves are enclosed by boundaries on *x*-and *y*-axes so that the airgap region Ω shown in Fig. 4 (a) does not have holes. It is noted that both curves are oriented positively. Employing the Green's theorem, the line integral that governs the airgap region Ω with magnetic vector potential field can be expressed as

$$\oint_C A_x(x, y)\,dx + A_y(x, y)dx = \iint_\Omega \left(A_{y_x} - A_{x_y}\right) d\Delta g \quad (2)$$

of which A_x and A_y have continuous first order partial derivative $\partial A_x / \partial y$ and $\partial A_y / \partial x$ respectively in the airgap region [1, 2, 3]. In 3D space the magnetic vector potential field *A* is expressed by

$$A(x, y, z) = A_x(x, y, z)a_x + A_y(x, y)a_y + A_z(x, y, z)\,a_z \quad (3)$$

The Green's theorem in vector form applied to magnetic vector potential is given by [2, 3]

$$\int_C A \cdot N\,ds = \iint_\Omega \nabla \cdot A\,d\Delta g \quad (4)$$

where *N* is the unit normal vector. The rotor of the SynRM3 is made up of stack laminations with different cut-off dimensions on the *q*-axis as shown in Fig. 4 (b). The 3D computation is essential for accurate analysis. Should the curve *C* in Fig.4 (b) be in the plane with bounding a volume *V*, (4) is then expressed as

$$\iint_V A \cdot N\,d\sigma = \iiint_V \nabla \cdot A\,dV \quad (5)$$

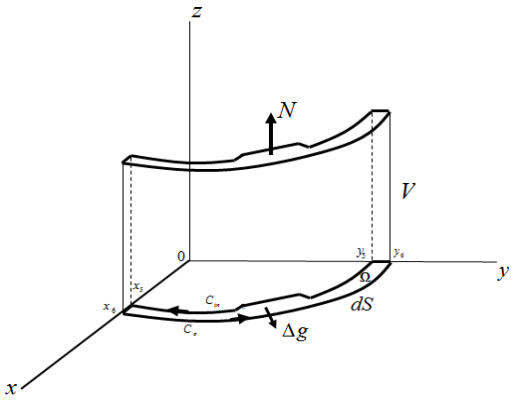

(a)

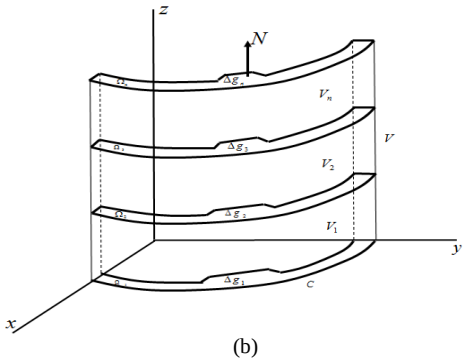

(b)

Fig.4. Lamination rotor stacks in 3D space, (a) single stack lamination with cut-off on the *q*-axis, (b) stack laminations having different cut-off dimensions on *q*-axis

The magnetic vector potential is divided by the airgap area Δg, and let the limit as Δg approaches zero, the curl of A normal to Δg at the point around which Δg shrinks to zero is obtained, and using the Kelvin-Stoke's theorem, the governing equations can be written as

$$\lim_{\Delta g \to 0} \frac{1}{\Delta g} \oint A \cdot ds = \nabla \times A \cdot a_Z = Curl_z\ A \tag{6}$$

$$\oint_C A \cdot dS = \iint_\Omega \nabla \times A \cdot d\Delta g \tag{7}$$

$$\iint_\Omega \nabla \times A \cdot d\Delta g = \iiint_V \nabla \times A \cdot dV \tag{8}$$

where dS is the vector differential length on the contour C bounding by the airgap area defined by Δg. It should be noted that the distribution of radial component of airgap flux density along the rotor periphery is very crucial in predicting the torque ripple [1]. The total magnetic core is made of main and leakage components. For the SynRM3, the magnetic vector potential is not constant along the transverse cross-section because of the reluctance variation in the axial direction of the airgap as shown in Fig.4 (b). The leakage flux of coils placed in stator slots will not be the same. The Kelvin-Stokes expression applied to the closed contour of the airgap of the SynRM3 in 3D space with bounding a volume V, is obtained by using the superposition principle and is written as

$$\begin{aligned} &\iint_{\Omega_1} \nabla \times A_1 \cdot d\Delta g_1 + \ldots + \iint_{\Omega_n} \nabla \times A_n \cdot d\Delta g_n \\ &\quad = \iiint_{V_1} \nabla \times A_1 \cdot dV_1 + \ldots + \iiint_{V_n} \nabla \times A_n \cdot dV_n \end{aligned} \tag{9}$$

III Finite Element Analysis Results

In this paper, a three-dimensional (3D) Finite Element Analysis (FEA) is performed using ANSYS 16.0 electromagnetic package. The flux density distribution and the inductances are numerically computed through the magnetostactic solver. A bounded domain $V = V_1 + V_2 + \ldots + V_n$ of the 3D space is considered and the equations that characterised the magnetostatic problem in domain V are well illustrated in [25]. In total, 450 SURA M250-35A lamination sheets are used to constitute the rotor core. Fig.5. shows the mesh plot on the surface of the rotor of the machine with sinusoidal rotor shape (SynRM3). A total number of 18076 tetrahedral elements are obtained for the rotor geometry with minimum edge length of 0.007857 *mm* on the low magnetic reluctance pole face (*d*-axis region), and with maximum edge length of 16.4495 *mm* on the high magnetic reluctance pole face (*q*-axis region). The efficiency, power factor and torque are obtained by using the magnetic-transient solver. The FEA models are carried out at constant speed and frequency of 1500-rpm and 50-Hz respectively.

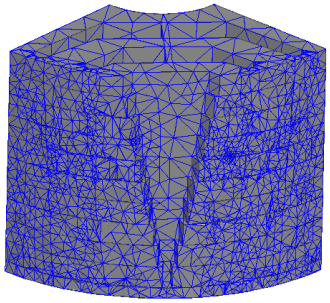

Fig.5. Mesh plot of rotor at full-load for SynRM3

A. *Flux density distribution*

Fig.6 shows the magnetic flux density distribution at full load plotted along the rotor periphery of the three different SynRMs.

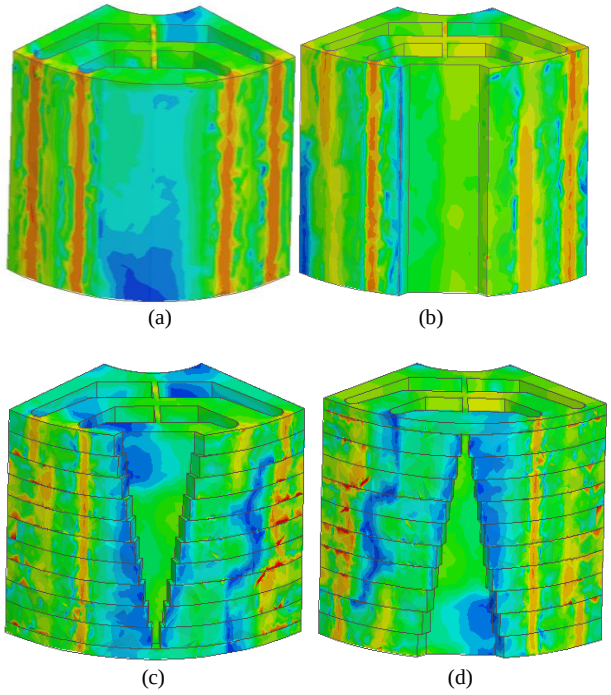

Fig.6. Airgap flux density distribution on the rotor periphery, (a) SynRM1, (b) SynRM2, (c) SynRM3, positive axial z-length, (d) SynRM3, negative axial z-length

Observing from Fig.6, it is visible that the tangential bridges are highly saturated in SynRM1 and SynRM2 than in SynRM3. On the other hand, , the flux density distribution in SynRM1 and SynRM2 is not seriouslly affected by the *q*-axis current. In contract, the *q*-axis current affects the flux density distribution in SynRM3. Fig. 7 (a) and (b) show the 3D airgap flux desity distribution on *d*-and *q*-axis for SynRM3. The machine operates with *d*-axis current of 1.247 A, dc and *q*-axis current of 7.904 A, dc.

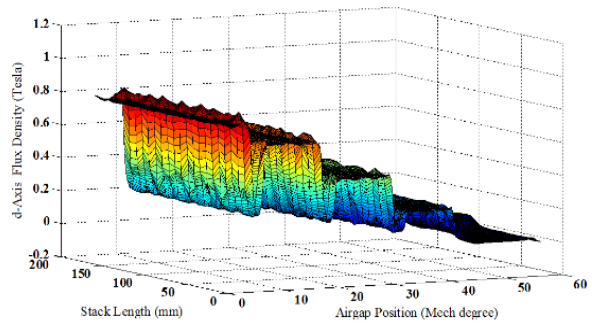

(a)

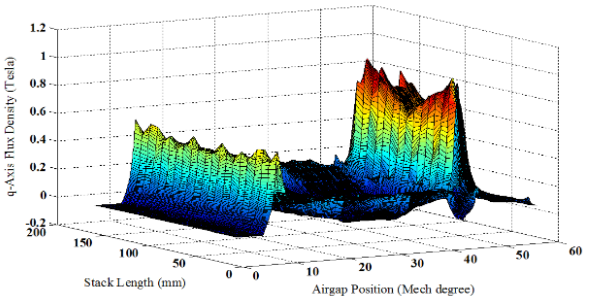

(b)

Fig.7. Airgap flux density distribution of the SynRM C, (a) *d*-axis, (b) *q*-axis

It is noticed that the stator slotting affects the airgap flux density distribution in both *d*-and *q*-axis. However, the non-uniformed distribution of airgap flux density on the *q*-axis due to variation of lamination shape along the stack length of SynRM1 is very noticeable and significant in Fig. 7 (b).

B. Performance Indexes at Maximum Power factor and Maximum Average Torque

The torque is directly related to the difference between the two axis magnetizing inductances $\Delta L_m = L_{md} - L_{mq}$, while the maximum apparent power factor ($APF_{\max}$) depends on the ratio of two-axis magnetizing inductances $\xi = L_{md} / L_{mq}$.

Table III provides the performance parameters at maximum average torque. These results were obtained from FEA at full-load (8A) condition. It should be noted that SynRM1 and SynRM2 attained their maximum torque at the current vector angle of 65º *elect* while the SynRM3 reached its maximum average torque at 60º *elect* (see Fig.8).

Observing from table III, it is evident that the SynRM3 has much lower torque ripple contents, but also a low power factor (*PF*) as compared to SynRM1 and SynRM2. The lower power factor of SynRM3 is due to lower saliency ratio and lower maximum torque field weakening ratio. Though, the machine with sinusoidal rotor shape (SynRM3) has reduced the torque ripple contents tremendously, and still maintains good average torque. The FEA results suggest that the machine will have a low inverter utilization factor due to low field weakening range.

TABLE III: PERFORMANCE PARAMETERS OF SYNRMS AT MAXIMUM AVERAGE TORQUE

Performance Indexes	**SynRMs Types**		
	SynRM1	***SynRM2***	***SynRM3***
L_{md} (mH)	603.9	598.1	581.6
L_{mq} (mH)	91.7	84.3	99.5
ΔL_m (mH)	512.2	513.8	482.1
ξ	6.6	7.1	5.8
T_{av} (Nm)	31.6	34.9	31.1
T_{ripple} (%)	17.6	41.9	6.4
APF (pu)	0.737	0.753	0.707
PF (pu)	0.734	0.809	0.68
η	92.3	92.9	92.8
$\delta\|_{\max \mathbf{T}}$	18.5º *elect*	17.2º *elect*	16.95º *elect*
$K\|_{\max \mathbf{T}}$	3.37	3.62	1.4º *elect*

Table IV depicts the performance parameters obtained from FEA, when the SynRMs operate at maximum airgap power factor. SynRM1 and SynRM2 reaches their airgap (apparent) power factor (*APF*) at the current vector angle of 70º *elect*.

TABLE IV: PERFORMANCE PARAMETERS OF SYNRMS AT MAXIMUM AIRGAP POWER FACTOR

Performance Indexes	**SynRMs Types**		
	SynRM1	***SynRM2***	***SynRM3***
L_{md} (mH)	624.8	598.3	599.4
L_{mq} (mH)	76.5	69.2	85.3
ΔL_m (mH)	548.3	529.1	514.1
ξ	8.2	8.6	7
T_{av} (Nm)	27.7	29.5	29.6
T_{ripple} (%)	20	45	6.9
$APF_{\max}$ (pu)	0.782	0.792	0.751
PF (pu)	0.686	0.75	0.654
η	90.7	91.2	91.7
$\delta\|_{\max \mathbf{PF}}$	19.1º *elect*	18.2º *elect*	17.4º *elect*
$K\|_{\max \mathbf{PF}}$	1.61	1.64	1.5

From Table IV, it is evident that SynRM1 and SynRM2 have high saliency ratio and high APF_{max}, but the first has a high ΔL_m with lower average torque, which does not corroborate with the torque equation theory. The drop in average torque of the machine without cut-off (SynRM1) is due to saturation of radial bridges caused by *q*-axis MMF. Furthermore, the SynRM3 has shown to have a low ΔL_m, but good average torque. Again, the FEA results do not validate the torque equation theory. The good average torque for the machine with sinusoidal rotor shape (SynRM3) is attributed to the fact that the radial bridges are not saturated at all by the *q*-axis MMF. It should be noted that the SynRM3 reached its APF_{max} at a current vector angle of 65º *elect*, not at 70º *elect* as in the case of SynRM1 and SynRM2. All three machines have a low maximum power factor field weakening ratio. They have a good efficiency especially when operating at maximum average torque.

C. Torque and Torque ripple as function of current angle

The electromagnetic torque developed by a SynRM can be computed with the airgap flux and magnetizing current using [22, 23, 24].

$$T = \frac{3}{2}\frac{p}{2}(L_{md} - L_{md})i_d i_q = \frac{3}{2}\frac{p}{2}(L_{md} - L_{md})I_m^2 \sin(2\theta) \quad (10)$$

Where θ is the current space vector angle, i_d and i_q are the *d*- and *q*-axis currents respectively, and I_m is the stator magnetizing current. The average torque profiles and torque ripple as function of current vector angle θ for different loadings are shown from Fig.8 to Fig. 10. Equation (10) shows that the torque is maximized for θ = 45^o *elect.* This does not correlate with the FEA results. With a current load of 8A, 6A and 4A, the average torque is maximized for θ = 65^o *elect*, θ = 60^o *elect and* θ = 55^o *elect* respectively, in both SynRM1 and SynRM2. For the machine with sinusoidal rotor shape (SynRM3), θ is shifted to a small value by 5^o *elect* for all three loading scenarios. The shift of θ to a small value in SynRM3 is due to less saturation of tangential bridges and unsaturated condition of radial bridges.

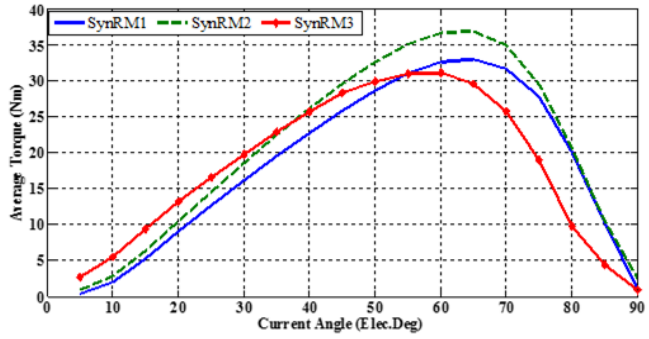

(a)

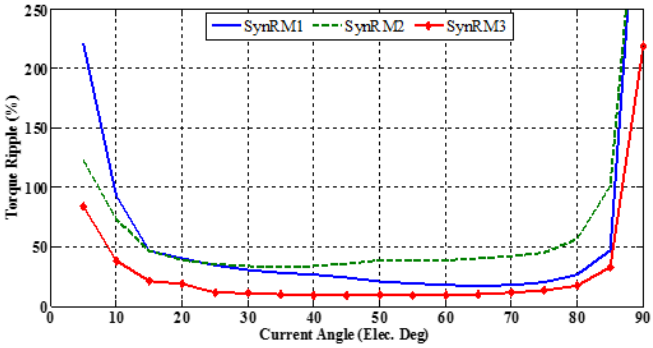

(b)

Fig. 8. Torque behavior ripple at 8 A (a) Torque as function of current angle, (b) Torque ripple as function of current angle.

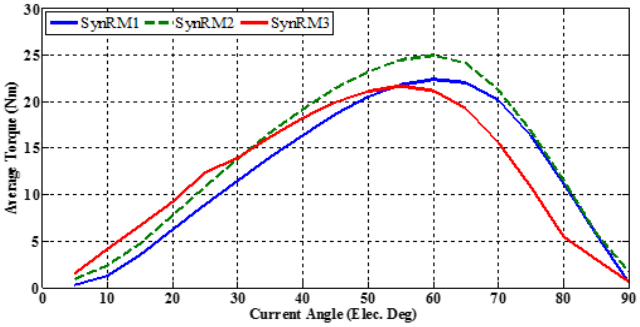

(a)

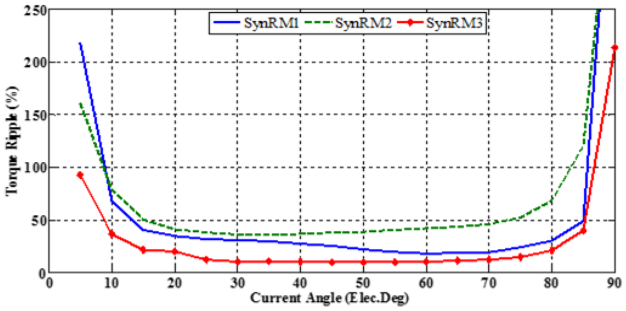

(b)

Fig. 9. Torque behavior ripple at 6 A (a) Torque as function of current angle, (b) Torque ripple as function of current angle.

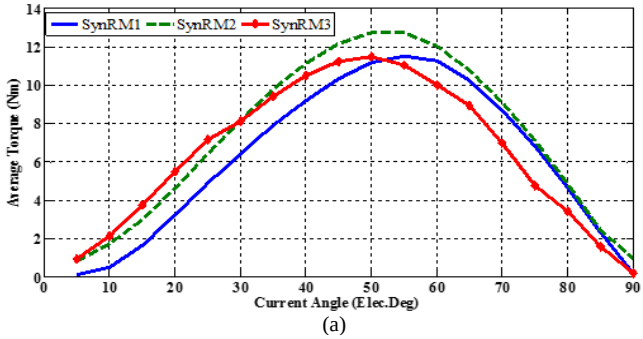

(a)

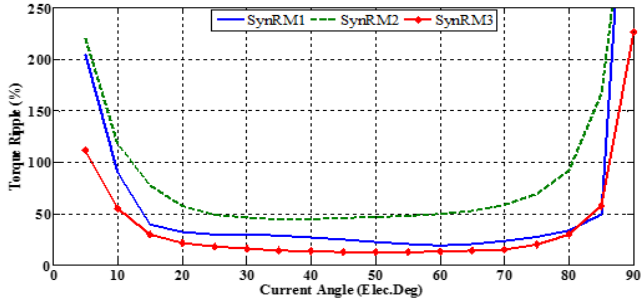

(b)

Fig. 10. Torque behavior ripple at 4 A (a) Torque as function of current angle, (b) Torque ripple as function of current angle.

Looking at the above torque profiles, it is clear that the current angle shifts to bigger values for maximum torque. This is mainly due to saturation effects. For I_s = 4 A, the maximum torque is closer to difference of *d*-axis and *q*-axis inductances as compared to I_s= 6 A and I_s = 8 A. The effect of current angle on torque ripple shows a different behavior. As expected, the torque ripple decreases with an increase in current angle. A low torque ripple is obtained between 20º *elect* and 70º *elect* for all three loading conditions. It is clear that the SynRM3 motor has tremendously reduced the torque ripple, either operating with maximum average torque or maximum apparent power factor, and the machine still maintains good average torque.

IV CONCLUSION

A 3D based Finite Element Analysis of a Synchronous Reluctance Motor with sinusoidal rotor lamination shape in the axial direction was performed. The governing expression of the airgap magnetic flux was derived from Kelvin-Stoke's theorem and the actual magnetic flux is obtained by employing the superposition principle. The magnetic flux is not calculated for unit depth and multiply by the stack length to find the actual magnetic flux in the machine as is always the case in electrical machines with plane symmetry. From FEA results the Synchronous Reluctance Motor with sinusoidal rotor lamination shape in the axial direction has proved to tremendously drop the torque ripple contents when operating with both maximum average torque and maximum apparent power factor. From the FEA results, it was clear that magnetic saturation contributes to the shift in current angle towards bigger values, thus the average torque is not maximized at 45º *elect* as expected.

Although, the machine with sinusoidal rotor shape has proven to provide better performance as far as torque characteristics are concerned, the FEA results have shown that the machine has a low power factor and low flux weakening range. Therefore, the inverter utilization factor will be low.

V REFERENCES

[1] W. Wang and B. Fahini, " *Comparative study of Electric Drives for EV/HEV propulsion system*", IEEE 2012 Electrical System for Aircraft, Railway and Ship Propulsion (ESARS), 16-18 Oct. 2012, Bologna, Italy

[2] V. Croitorescu, I. Croitorescu and G Danciu, " Functional modelling of an electric machine used on road vehicles", 8th International Symposium on advanced topics in electrical engineering, May 23-24, 2013, Bucharest, Rumania.

[3] F. N. Jurca, R. Mircea, C. Martis, R. Martis and P. P. Florin, " Synchronous reluctance motors for small electric traction vehicle", 2014 International Conference and Exposition on Electrical and Power Engineering (EPE 2014), 16-18 October, Iasi, Romania.

[4] J. Lin, K. W. E. Cheng, Z. Zhang and X. Xue, " Experimental investigation of in-wheel reluctance motor driving system for future electric vehicles", 3rd International conference on Power Electronics Systems and Applications, 2009.

[5] S. Taghavi and P. Pillay, "A mechanically robust rotor with transverse-laminations for a synchronous reluctance machine for traction applications", 2014.

[6] N. Bianchi, S. Bolognani, D. Bon, and M. D. Pre', Rotor Flux-barrier Design for Torque Ripple Reduction in Synchronous Reluctance and PM-Assisted Synchronous Reluctance Motors. IEEE Trans. on Ind. Appl., vol. 45, Issue 3, May-June 2009, pp. 921-928.

[7] N. Bianchi, S. Bolognani, D. Bond and M. D. Pre', Rotor Flux-barrier Design for Torque Ripple Reduction in Synchronous Reluctance Motors. *Proc. 41th IEEE Conf. On Industry Applications*, 2006, 1193-1200.

[8] E.C Lovelace, "Optimization of a magnetically saturable IPM Sync. Mac. Drive", PhD, Dept. of Elec. Eng. & Comp. Sci., MIT, 2000.

[9] R. R. Fessler and M. Olszewski. "*Assessment of Motor Technologies for Traction Drives of Hybrid and Electrical Vehicles*", USA Department of Energy, FreedomCar and Vehicle Technologies Mar 2011.

[10] N. Bianchi and S. Bolognani, A Consoli, T. M. Jahns, R. D. Lorenz, E. C. Lovelace, S. Morimoto and A. Vagati, "Design Analysis and Control of Interior Permanent Magnet Synchronous Machines". *Proceeding of International Conference on Electrical Machines, ICEM.* Aug. Helsinki, 2000.

[11] E. Armando, P. Guglielmi, G. Pellegrino, M. Pastorelli and A. Vagati, "Accurate Modelling and Perf. Anal. of IPM-PMASR Motors". *IEEE Trans. on Ind. Appl.*, vol. 45, Issue 1, Jan-Feb 2009, pp. 123-130.

[12] M. J Kamper, F. S. Van der Merwe and S. Williamson, "Direct finite element design optimization of the cage-less reluctance synchronous machine", *IEEE Trans. on Energy Con.*, Vol. 11, IS, 3, Sept. 1996, pp: 547-555.

[13] M. Sanada, K. Hiramato, S. Morinoto, and Y. Takeda. "Torque Ripple Improvement for Synchronous Reluctance Motor Using Asymmetric Flux Barrier Arrangement". *Proc. IEEE Ind. App. Soc. Annual Meeting*, 12-16 Oct. 2003.

[14] M. Muteba, B. Twala and D. Nicolae "Torque Ripple Minimization in Synchronous Reluctance Motor Using a Sinusoidal Rotor Lamination Shape", *Proc. of the Int. Conf. on Elect. Machines*, ICEM, 2016, Sep 4-7, 2016, Lausanne, Switzerland.

[15] I. Boldea and L. Tutelea, "Electric Machines: Steady State, Transients and Design with Matlab", *Taylor and Francis*, 2010.

[16] W. H. Hayt, JR. "Engineering Electromagnetics", *MacCraw-Hill International Editions*, 1981.

[17] J. D. Kraus," Electromagnetics" *MacCraw-Hill International Editions*, 1991

[18] W. Zhao, T. A Lipo and B. Kwon "Material-efficiency magnet shape for torque pulsation minimization in synchronous permanent motors". *IEEE Trans. On Industrial Electronics*, vol. 61, Issue 10, 2014, pp. 5579-5787.

[19] I**.** Boldea, "Reluctance Synchronous Machines and Drives" *Oxford Science Publications*, 1st edition, Aug 1996.

[20] A. Vagati, G. Franceschini, I Morongiu and G.P. Troglia, "Design criteria of high performance synchronous reluctance motors". Ind. Appl., Annual Meet. 4-9 Oct., 1992, Vol.1, pp: 66-73.

[21] R. R. Moghaddam, "Synchronous reluctance machine (SynRM) design", Master Thesis, Stockholm, 2007.

[22] A. Vagati, "*The Synchronous Reluctance Solution*: *A New Alternative in a.c. Drives*", 20th Conference on Industrial Electronics, Control and Instrumentation, IECON'94, 5-9 Sept. 1994, Bologna, Italy.

[23] T.A. Lipo, T. J.E Miller, A. Vagati, I. Boldea, L. Malesani and T. Fukao, "*Synchronous Reluctance Drives"*, Tutorial IEEE-IAS Annual Meeting, Denver, CO, Oct. 1994

[24] J. Haataja, "*A comparative study of four-pole induction motors and synchronous reluctance motors in variable speed drives*", Lappeenranta University of Technology, ISBN 951-764-772, ISSN 1456-4491, 2003.

[25] M.V. Ferreira da Luz, E. Deschamps, F. Runcos and S.L. Nau, Analysis of 65 kVA high efficiency synchronous generator using finite element Method", *Proc. of the XII Int. Sym. on Electromagnetic Fields in Mechatronics*, Electrical and Electronic Engineering (ISEF), Spain, 2005.